



## Surface strain rates and crevassing of Campbell Glacier Tongue in East Antarctica analysed by tide-corrected DInSAR

Hyangsun Han & Hoonyol Lee

To cite this article: Hyangsun Han & Hoonyol Lee (2017) Surface strain rates and crevassing of Campbell Glacier Tongue in East Antarctica analysed by tide-corrected DInSAR, Remote Sensing Letters, 8:4, 330-339, DOI: [10.1080/2150704X.2016.1271158](https://doi.org/10.1080/2150704X.2016.1271158)

To link to this article: <http://dx.doi.org/10.1080/2150704X.2016.1271158>



Published online: 22 Dec 2016.



Submit your article to this journal [↗](#)



Article views: 41



View related articles [↗](#)



View Crossmark data [↗](#)

# Surface strain rates and crevassing of Campbell Glacier Tongue in East Antarctica analysed by tide-corrected DInSAR

Hyangsun Han <sup>a</sup> and Hoonyol Lee <sup>b</sup>

<sup>a</sup>Unit of Arctic Sea-Ice Prediction, Korea Polar Research Institute, Incheon, Republic of Korea; <sup>b</sup>Division of Geology and Geophysics, Kangwon National University, Chuncheon, Republic of Korea

## ABSTRACT

This research presents the measurement of surface strain rates over Campbell Glacier Tongue (CGT) in East Antarctica from tide-corrected ice velocity derived by removing the vertical tidal deflection from the 14 COSMO-SkyMed 1-day differential interferometric synthetic aperture radar images obtained in 2011. The hinge zone of CGT shows large longitudinal, transverse, shear, and vertical strain rates, especially in a heavy crevassing band, while the freely floating zone shows very small strain rates. This represents that the surface deformation by ice flow in the hinge zone is significantly larger than that in the freely floating zone. The orientations of crevasses in the hinge zone agree reasonably well with the directions orthogonal to the axes of the most tensile strain rates calculated from the tide-corrected ice velocity, which demonstrates that the crevassing is attributed to the gravitational ice flow rather than to the tidal flexure.

## ARTICLE HISTORY

Received 21 June 2016  
Accepted 7 December 2016

## 1. Introduction

Surface strain rates of a glacier are critical to the understanding rheological properties and deformation mechanism of ice. Particularly, they play a role as a primary indicator of the formation of crevasses that are common features on the glacial surface. Crevassing of floating glaciers such as ice shelves and glacier tongues considerably influences ice calving and mass discharge (Benn, Hulton, and Mottram 2007; Nick et al. 2010). Crevasses on the grounded ice streams are formed by stresses resulting from ice flow (Vaughan 1993; Price and Whillans 2001). However, it is difficult to determine whether the deflection of ice body by tide contributes to the crevassing of floating glaciers that experience both the gravitational ice flow and tidal flexure (Han and Lee 2014, 2015). Therefore, accurate measurement of surface strain rates of a floating glacier is essential to analyse its ice dynamics.

The surface strain rates of glaciers can be calculated from ice velocity field. Differential interferometric synthetic aperture radar (DInSAR) has been widely used to map ice velocity over glaciers (Rignot, Mouginot, and Scheuchl 2011; Han and Lee 2015). For the Antarctic floating glaciers, DInSAR pairs with short temporal baseline such as 1 day are needed to map ice velocity because most of them flow fast and thus large temporal decorrelation of ice surface can occur even in a few days (Han and Lee 2014). The DInSAR signals over the

floating glaciers include not only the gravitational flow in the horizontal direction but also the vertical deflection due to sea surface tilt by tide (Han and Lee 2014, 2015). As the magnitude of daily tide variation can be similar to that of 1-day ice flow, the vertical tidal deflection signals should be removed from the DInSAR images to measure accurate ice velocity and strain rates. However, the measurement of strain rates over a floating glacier from DInSAR images have been challenging so far because the tidal deflection significantly varies both spatially and temporally, especially in the hinge zone.

The spatial variations of the vertical tidal deflection can be investigated by using tide deflection ratio defined as the ratio of tidal deflection over tide height (Han and Lee 2014). The tide deflection ratio can be determined by double-differential interferometric SAR (DDInSAR) technique that differentiates two DInSAR images by assuming constant gravitational ice flow during the observations (Han and Lee 2014, 2015). It allows the measurement of tide-corrected ice velocity and strain rates of floating glaciers from DInSAR images.

In this research, we measure surface strain rates over Campbell Glacier Tongue (CGT) in East Antarctica from tide-corrected ice flow velocity derived by removing the vertical tidal deflection from a series of 1-day DInSAR images, and analyse ice deformation properties and crevassing mechanism of CGT.

## 2. Materials and methodology

### 2.1. Study area

CGT is a seaward extension of Campbell Glacier, which flows into the Northern Terra Nova Bay in Ross Sea, East Antarctica (Figure 1(a)). CGT is composed of two ice streams: one is the main stream in the east and the other is the branch stream composed of broken ice chunks in the west. Many crevasses parallel to the long axis of CGT are formed in the hinge zone. Annual ice velocity of CGT was 180–260 m year<sup>-1</sup> measured by the offset tracking of the COSMO-SkyMed synthetic aperture radar (SAR) images between 2010 and 2011 (Han, Ji, and Lee 2013). The vertical tidal deflection of CGT is approximately 60 cm (Han and Lee 2014) which is similar to the distance that the ice flows in a day.

### 2.2. Data set

A total of 14 one-day DInSAR pairs over CGT were obtained from January to November 2011 by COSMO-SkyMed satellites equipped with X-band SAR to measure ice velocity and strain rates through the year (Table 1). All the SAR images were acquired in strip-map mode (3 m spatial resolution), VV-polarization, and an incidence angle of 40° in descending orbit. Global Digital Elevation Model (GDEM) of the Advanced Spaceborne Thermal Emission and Reflection Radiometer (Fujisada et al. 2005) was used to remove topographic phases from the 1-day interferograms. The vertical accuracy of the GDEM is 20 m which is enough to remove topographic phases from the interferograms due to very short perpendicular baselines of the DInSAR pairs (Table 1).

Ross Sea Height-Based Tidal Inverse Model (Ross\_Inv) (Padman, Erofeeva, and Joughin 2003) was used to predict tide height at a centre point of the freely floating zone of CGT (a red point in Figure 1(a)). The load tide effect on the predicted tide height was corrected by Topography Experiment/Poseidon global inverse load tide model (TPXO

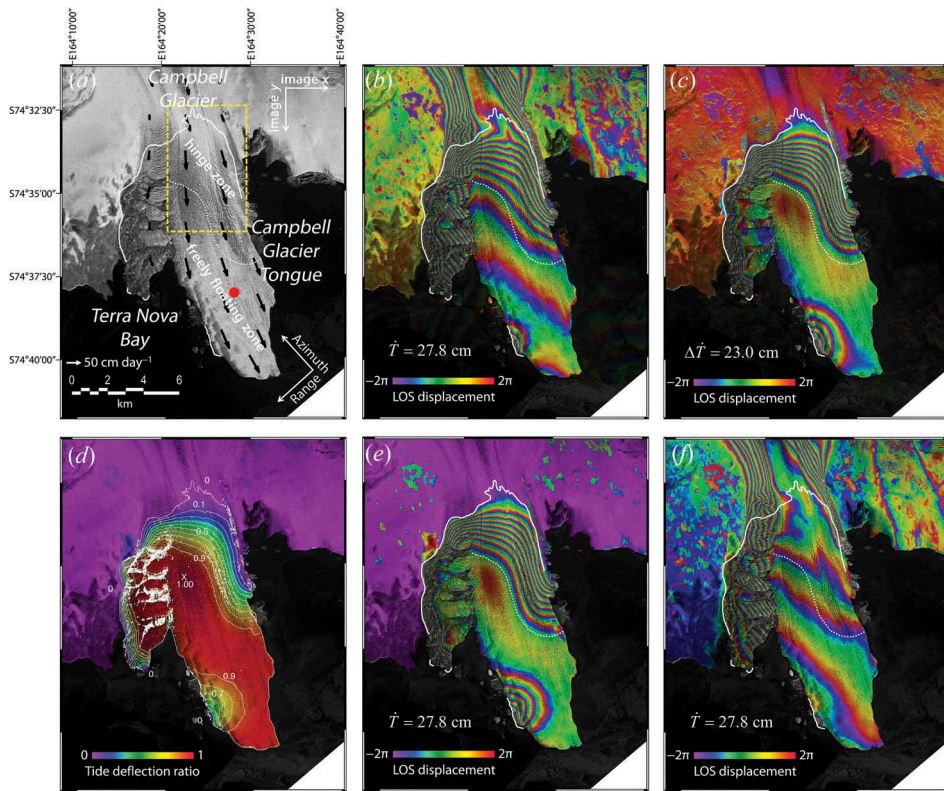


**Figure 1.** (a) COSMO-SkyMed SAR image over CGT obtained on 27 November 2011. A yellow dotted box represents a heavy crevassing area. (b) An example of the 1-day DInSAR and (c) DDInSAR image. (d) Map of tide deflection ratio ( $a$ -map). (e) The vertical tidal deflection and (f) tide-corrected ice flow in LOS direction for the DInSAR image of (b). The white lines represent the location of the grounding line and the white dotted line represents the seaward edge of the hinge zone (Han and Lee 2014).

**Table 1.** COSMO-SkyMed 1-day DInSAR image pairs used in this research.

ID	Dates of master, slave	Perpendicular baseline (m)	1-day tide difference, $\dot{T}$ (cm)
1	26 January 2011, 27 January 2011	18.9	-11.6
2	27 February 2011, 28 February 2011	5.7	-4.5
3	15 March 2011, 16 March 2011	-44.4	-17.5
4	31 March 2011, 1 April 2011	-39.2	8.3
5	2 May 2011, 3 May 2011	-89.6	8.3
6	18 May 2011, 19 May 2011	75.9	27.8
7	3 June 2011, 4 June 2011	-36.5	-3.3
8	19 June 2011, 20 June 2011	-47.5	-14.7
9	22 August 2011, 23 August 2011	181.7	27.6
10	7 September 2011, 8 September 2011	37.3	1.0
11	9 October 2011, 10 October 2011	-44.4	5.8
12	25 October 2011, 26 October 2011	-110.9	-14.0
13	10 November 2011, 11 November 2011	-91.7	2.0
14	26 November 2011, 27 November 2011	-23.4	7.5

6.2 Load Tide model) (Egbert and Erofeeva 2002). The inverse barometer effect (IBE) on the predicted tide height, i.e., sea level drop of about 1 cm per increase in barometric pressure of 1 mbar, was corrected by using *in situ* atmospheric pressure measured by an automatic weather system installed near CGT.

### 3. Methodology

This section describes how tide-corrected ice flow velocity and surface strain rates of CGT are measured from DInSAR images. First, the surface deformation in the line of sight (LOS) direction was extracted from the 14 one-day DInSAR images. Figure 1(b) is an example of the DInSAR image with the 1-day tide variation of 27.8 cm predicted by the IBE-corrected Ross\_Inv (ID 6 in Table 1). The DInSAR signals over CGT include both the gravitational ice flow ( $\phi_{\text{flow}}^{\text{LOS}}$ ) and the vertical tidal deflection ( $\phi_{\text{tide}}^{\text{LOS}}$ ). The  $\phi_{\text{tide}}^{\text{LOS}}$  can be presented as a function of coordinates  $x$  and  $y$  in the horizontal plane and time  $t$  by (Han and Lee 2015)

$$\phi_{\text{tide}}^{\text{LOS}}(x, y, t) = \alpha(x, y)\dot{T}(x, y, t) \cos \theta(x, y), \quad (1)$$

where  $\alpha$  is the tide deflection ratio,  $\dot{T}$  is tide variation during the 1-day DInSAR observation, and  $\theta$  is the radar look angle, respectively.

To find  $\alpha$  over CGT, we generated a total of 91 DDInSAR images from the 14 DInSAR images and extracted the vertical tidal deflection of CGT. Figure 1(c) shows an example of the DDInSAR image with the tide variation during the observation ( $\Delta\dot{T}$ ) of 23.0 cm, which was generated by differentiating the DInSAR pair of ID 4 from that of ID 8 in Table 1. The DDInSAR images clearly showed the location of grounding line and the spatial variation of the tidal deflection while fringes over grounded ice stream disappeared completely. This confirms that an assumption of the DDInSAR, i.e., the constant gravitational ice flow during the observations, is valid. A map of  $\alpha$  over CGT was generated by performing the pixel-based linear regression between the DDInSAR-derived tidal deflection and  $\Delta\dot{T}$  during the DDInSAR observations (Han and Lee 2014) (Figure 1(d)). The  $\alpha$ -map has 3.7% uncertainty which would be mainly originated from the error of the IBE-corrected Ross\_Inv. Such uncertainty is very similar to that of the  $\alpha$ -map from a previous research (Han and Lee 2014) (4.4%) which used 120 DDInSAR images from 16 one-day InSAR pairs obtained during 2010–2011.

$\phi_{\text{tide}}^{\text{LOS}}$  of CGT corresponding to each 1-day DInSAR image was estimated using Equation (1), which was then removed from the DInSAR signals to extract the 1-day  $\phi_{\text{flow}}^{\text{LOS}}$ . Figure 1(e,f) shows  $\phi_{\text{tide}}^{\text{LOS}}$  and  $\phi_{\text{flow}}^{\text{LOS}}$  for the DInSAR image of Figure 1(b), respectively.  $\phi_{\text{flow}}^{\text{LOS}}$  was converted into the local flow direction (black arrows in Figure 1(a)) estimated by the offset tracking between two SAR images obtained on 25 October and 10 November 2011 (Han, Ji, and Lee 2013). To represent an annual state of ice velocities, we generated the maps of the averaged tide-corrected ice velocity ( $\mathbf{v}$ -map) and its standard deviation ( $\sigma_{\mathbf{v}}$ -map) from the 14 tide-corrected 1-day ice flows.

The flow-oriented surface strain rates such as longitudinal ( $\dot{\epsilon}_{\parallel}$ ), transverse ( $\dot{\epsilon}_{\perp}$ ), shear ( $\dot{\epsilon}_{s}$ ), and the vertical strain rate ( $\dot{\epsilon}_{v}$ ) were calculated by (Bindschadler et al. 1996)

$$\begin{aligned} \dot{\epsilon}_{\parallel} &= \dot{\epsilon}_{xx} \cos^2 \beta + 2\dot{\epsilon}_{xy} \sin \beta \cos \beta + \dot{\epsilon}_{yy} \sin^2 \beta, \\ \dot{\epsilon}_{\perp} &= \dot{\epsilon}_{xx} \sin^2 \beta - 2\dot{\epsilon}_{xy} \sin \beta \cos \beta + \dot{\epsilon}_{yy} \cos^2 \beta, \\ \dot{\epsilon}_{s} &= (\dot{\epsilon}_{yy} - \dot{\epsilon}_{xx}) \sin \beta \cos \beta + \dot{\epsilon}_{xy} (\cos^2 \beta - \sin^2 \beta), \\ \dot{\epsilon}_{v} &= -(\dot{\epsilon}_{\parallel} + \dot{\epsilon}_{\perp}), \end{aligned} \quad (2)$$

where  $\dot{\epsilon}_{xx}$ ,  $\dot{\epsilon}_{yy}$ , and  $\dot{\epsilon}_{xy}$  are the strain rates with respect to the directions,  $x$  and  $y$ , corresponding to the images axes calculated from the  $\mathbf{v}$ -map, and  $\beta$  is the local flow direction estimated by the offset tracking, measured counterclockwise from the image

$x$ -axis. The derivation of Equation (2) is described in detail in the Appendix of Bindshadler et al. (1996). Longitudinal crevasses form parallel to flow line in an ice divergence zone where  $\dot{\epsilon}_t$  is very large. Transverse crevasses that stretch across the flow line form in a longitudinal extension zone showing large  $\dot{\epsilon}_l$ . Splashing crevasses form in a shearing zone and are concave up with respect to local flow. Crevasses are typically parallel to the least tensile principal strain rate ( $\dot{\epsilon}_1$ ) axes and normal to the most tensile principal strain rate ( $\dot{\epsilon}_2$ ) axes in the horizontal plane (Harper, Humphrey, and Pfeffer 1998). We computed the axes of the principal strain rates by using the surface strain rates (Harper, Humphrey, and Pfeffer 1998) to compare with the orientations of the crevasses on CGT.

## 4. Results and discussion

### 4.1. Tide-corrected ice velocity of CGT

Prior to the generation of tide-corrected ice velocity map, we assessed the effect of the vertical tidal deflection on the measurement of ice velocity. Figure 2(a) shows the ice velocity of CGT derived from the DInSAR image without compensating for the tidal variation ( $\dot{T}$  of 27.8 cm) during the InSAR acquisition as shown in Figure 1(b). The ice velocity in the freely floating zone of CGT is approximately  $90 \text{ cm day}^{-1}$  which is about 1.3 times faster than that measured by the offset tracking of the SAR images (about  $70 \text{ cm day}^{-1}$ ) obtained in the same year of the DInSAR observations (Han, Ji, and Lee 2013). The magnitude of the velocity difference in the freely floating zone (20 cm) corresponds to the horizontal displacement converted from the vertical tidal deflection of about 27 cm. This demonstrates that the vertical tidal deflection should be removed from DInSAR signals in order to measure accurate ice velocity over floating glaciers.

Figure 2(b,c) shows the  $\mathbf{v}$ -map and  $\sigma_v$ -map, respectively. Over the main stream of CGT, the ice velocity gradually increased from the grounding line ( $52 \text{ cm day}^{-1}$ ) to the ice front ( $67 \text{ cm day}^{-1}$ ), and from margins to the central flow line of the glacier tongue. The tide-corrected ice velocity over CGT is approximately similar to the offset tracking measurements (Han, Ji, and Lee 2013). Most areas of the main stream of CGT show small

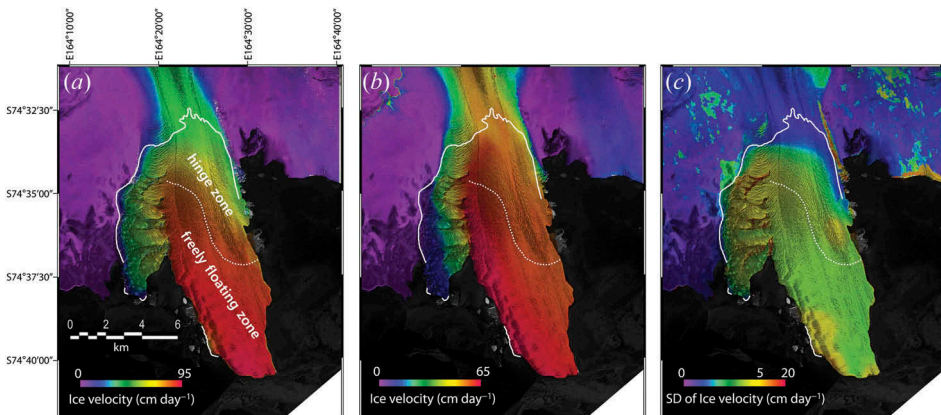


**Figure 2.** (a) Map of the ice velocity of CGT generated from the DInSAR image with  $\dot{T}$  of 27.6 cm. Maps of (b) the averaged tide-corrected ice velocity of CGT and (c) its standard deviation (SD) derived from the tide-corrected 1-day ice flows.

$\sigma_v$  values less than  $4 \text{ cm day}^{-1}$  (Figure 2(c)), which accounts for only 5% of the maximum ice velocity of CGT. The branch stream of CGT shows larger  $\sigma_v$  values than the main stream due to the irregular ice flow of the broken ice chunks (Han and Lee 2015).

#### 4.2. Tide-corrected strain rates and crevasses of CGT

The flow-oriented surface strain rates were calculated from the  $\mathbf{v}$ -map using Equation (2). Figure 3 shows the maps of  $\dot{\epsilon}_l$ ,  $\dot{\epsilon}_t$ ,  $\dot{\epsilon}_s$ ,  $\dot{\epsilon}_v$ , and uncertainties in the  $\dot{\epsilon}_l$  and  $\dot{\epsilon}_v$  over CGT, respectively. The uncertainties in the strain rates were propagated from the uncertainties in  $\mathbf{v}$ -map, i.e.,  $\sigma_v$  values. The uncertainties in  $\dot{\epsilon}_l$  (Figure 3(e)) are similar to those in  $\dot{\epsilon}_t$  and  $\dot{\epsilon}_s$ . In the branch stream of CGT, the strain rates have large uncertainties due to the random motion of the broken ice chunks (Han and Lee 2014), and thus they are not analysed in this research.

Most of the main stream of CGT showed positive  $\dot{\epsilon}_l$  values representing ice extension by increasing ice velocity along the flow lines (Figure 3(a)). Within the hinge zone, the mean value of  $\dot{\epsilon}_l$  was  $0.23 \times 10^{-4} \pm 0.03 \times 10^{-4} \text{ day}^{-1}$  which is higher than that in the freely floating zone ( $0.07 \times 10^{-4} \pm 0.01 \times 10^{-4} \text{ day}^{-1}$ ). This is because the ice stretched in the hinge zone due to the increasing ice velocity along the flow line, while the freely floating zone showed almost constant velocity. The formation of crevasses in the hinge zone would be little influenced by the extension of ice surface in the region because

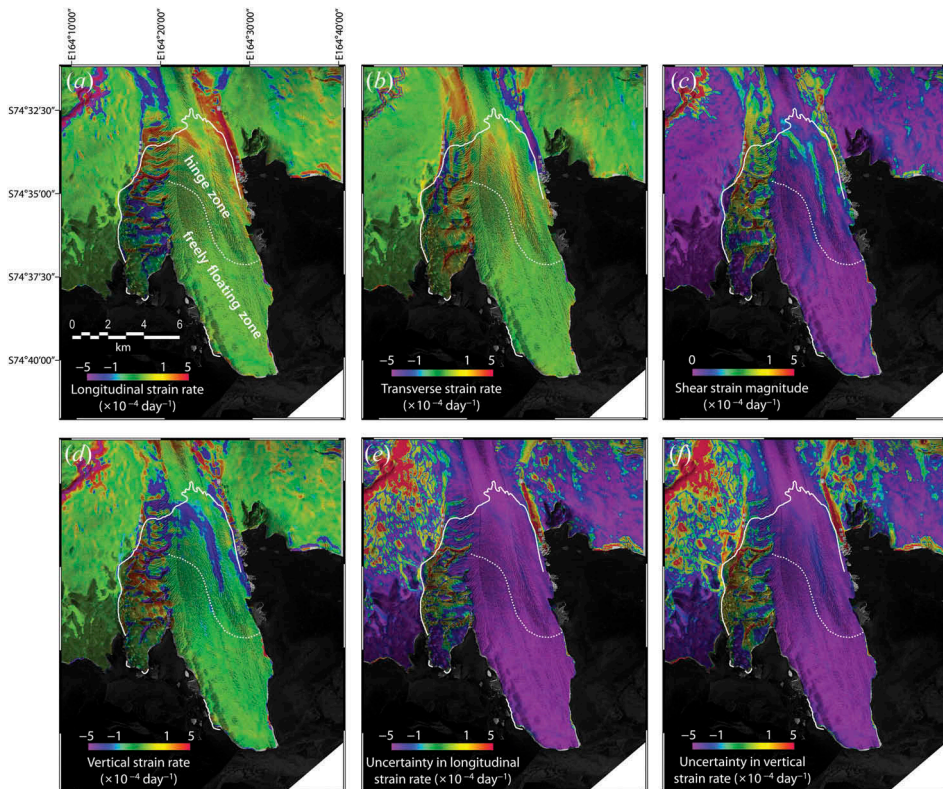


**Figure 3.** Maps of (a) longitudinal, (b) transverse, (c) magnitude of shear, and (d) vertical strain rate over CGT, and (e) the uncertainty in the longitudinal strain rate and (f) in the vertical strain rate.

they formed parallel to local flow (Figure 1(a)). This suggests that  $\dot{\epsilon}_t$  values representing large ice divergence can be higher than  $\dot{\epsilon}_l$  values in the region.

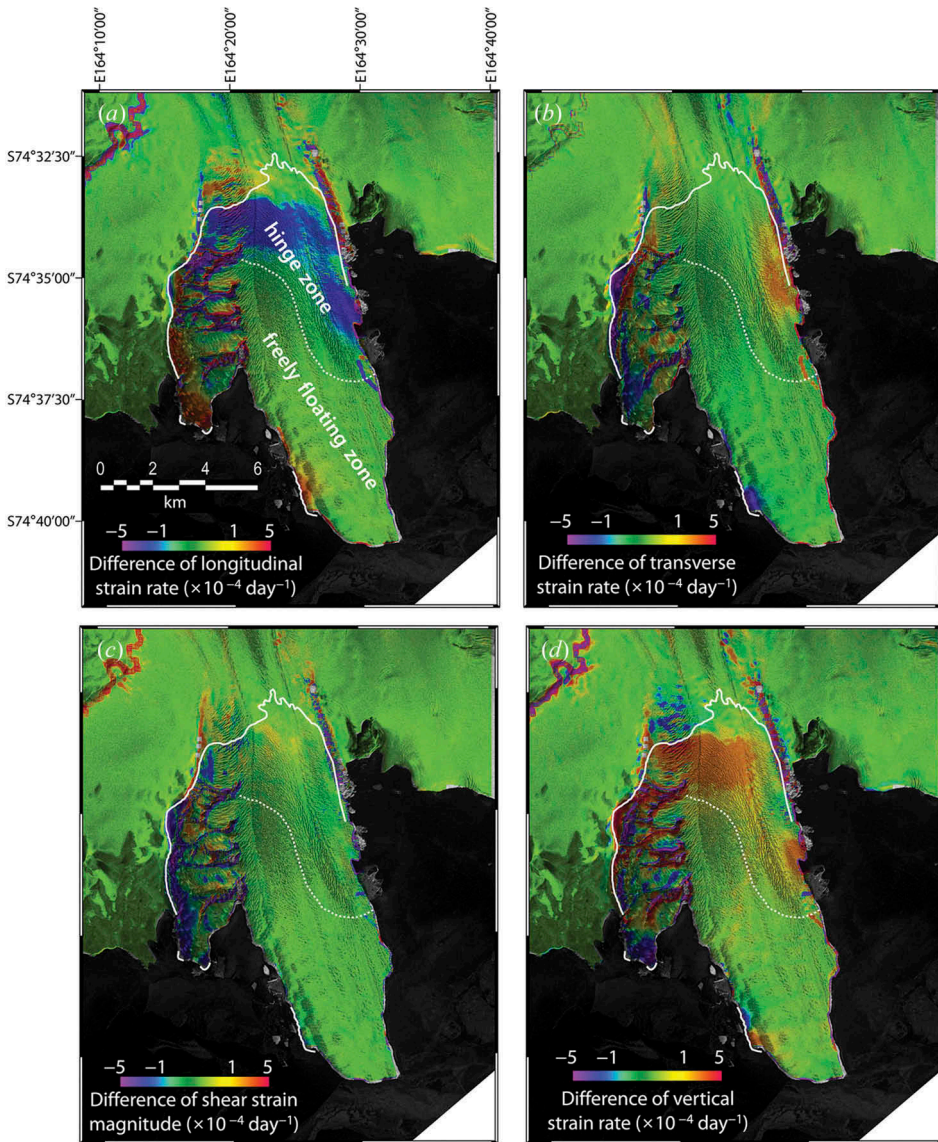
The  $\dot{\epsilon}_t$ -map (Figure 3(b)) clearly shows the ice convergence (positive  $\dot{\epsilon}_t$  values) and divergence (negative  $\dot{\epsilon}_t$  values) regions. The hinge zone showed the mean  $\dot{\epsilon}_t$  value of  $0.30 \times 10^{-4} \pm 0.05 \times 10^{-4} \text{ day}^{-1}$ . Large ice divergence was observed in the centre of the hinge zone where the  $\dot{\epsilon}_t$  values were estimated up to  $1 \times 10^{-4} \text{ day}^{-1}$ . This represents that ice spreads out from the central hinge zone. Such ice divergence zone coincides with a crevassing band, which verifies that the type of crevasses is the longitudinal crevasses. In the freely floating zone, the  $\dot{\epsilon}_t$  values are very small with the mean value of  $0.08 \times 10^{-4} \pm 0.02 \times 10^{-4} \text{ day}^{-1}$  and few crevasses are observed due to spatially constant ice velocity.

Figure 3(c) shows the magnitude of  $\dot{\epsilon}_s$  over CGT. High  $\dot{\epsilon}_s$  values are observed in the hinge zone with the mean value of  $0.18 \times 10^{-4} \pm 0.03 \times 10^{-4} \text{ day}^{-1}$ , especially in the heavy crevassing band (approximately  $0.5 \times 10^{-4} \text{ day}^{-1}$ ) due to the shearing by the lateral drag at the eastern part of CGT (Han and Lee 2014). However, the  $\dot{\epsilon}_s$  values in the crevassing band are only half the magnitudes of  $\dot{\epsilon}_t$  values in the region, which represents that the crevasses are more influenced by ice divergence than shearing. The  $\dot{\epsilon}_s$  values in the freely floating zone are very small with the mean value of  $0.03 \times 10^{-4} \pm 0.01 \times 10^{-4} \text{ day}^{-1}$  due to little lateral drag.

The longitudinal crevasses in the hinge zone should move downstream by the ice flow. However, the crevasses disappeared in the freely floating zone, which may be due to ice surface ablation, refreezing meltwater, or infilling with snow (Harper, Humphrey, and Pfeffer 1998). The freely floating zone showed very low strain rates so that chances of forming new crevasses in the region are infinitesimal.

The whole area of the main stream of CGT showed negative  $\dot{\epsilon}_v$  values representing ice thinning by flow (Figure 3(d)). The mean  $\dot{\epsilon}_v$  value of the hinge zone was  $-0.54 \times 10^{-4} \pm 0.08 \times 10^{-4} \text{ day}^{-1}$  of which the magnitude is 3.6 times larger than that of the freely floating zone ( $-0.15 \times 10^{-4} \pm 0.04 \times 10^{-4} \text{ day}^{-1}$ ). The crevassing band in the hinge zone showed large ice thinning with the  $\dot{\epsilon}_v$  value of about  $-2.5 \times 10^{-4} \text{ day}^{-1}$  due to the extremely stretching and diverging ice surface. Considering an ice thickness value of  $340 \pm 18 \text{ m}$  for CGT measured by the Geoscience Laser Altimetry System onboard the Ice, Cloud, and land Elevation Satellite (Han and Lee 2015), the mean annual thinning by ice flow in the hinge zone and the freely floating zone were estimated to be  $6.70 \pm 1.09 \text{ m year}^{-1}$  and  $1.86 \pm 0.29 \text{ m year}^{-1}$ , respectively. However, the ice thinning rates may be erroneous as a result of the constant ice thickness over the whole CGT (Han and Lee 2015). The uncertainties in  $\dot{\epsilon}_v$  (Figure 3(f)) were slightly larger than those in other strain rates (Figure 3(e)) because they were propagated from the uncertainties in both  $\dot{\epsilon}_l$  and  $\dot{\epsilon}_t$ . However, it accounts for only about 10% of the magnitudes in the  $\dot{\epsilon}_v$  values.

We evaluated the effect of the vertical tidal deflection on the measurements of the strain rates. Figure 4 shows the difference of  $\dot{\epsilon}_l$ ,  $\dot{\epsilon}_t$ ,  $\dot{\epsilon}_s$ , and  $\dot{\epsilon}_v$  derived from the tide-corrected (Figure 2(b)) and tide-uncorrected ice velocities (Figure 2(a)) (i.e., tide-corrected strain rates minus tide-uncorrected strain rates). The differences were very small over grounded ice, while large differences were observed in the hinge zone, except for  $\dot{\epsilon}_s$  due to its very low magnitudes, rather than the freely floating zone. This is because the vertical tidal deflection contained in the tide-uncorrected velocities, causing preposterous strain rates, varies spatially in the hinge zone. This result indicates again that the vertical tidal deflection should be removed from DInSAR signals to measure accurate strain rates of floating glaciers.



**Figure 4.** The difference of (a) longitudinal, (b) transverse, (c) magnitude of shear, and (d) vertical strain rate from the tide-corrected and the tide-uncorrected ice velocities.

Figure 5 shows axes of  $\dot{\epsilon}_1$  and  $\dot{\epsilon}_2$  at 20 large crevasses in the hinge zone of CGT (a yellow box in Figure 1(a)) and the comparisons of the crevasse orientations with the  $\dot{\epsilon}_1$  axes, measured by counterclockwise from the image x-axis from the tide-uncorrected ice velocities (Figure 2(a)) and tide-corrected ice velocities (Figure 2(b)), respectively. The crevasse orientations did not agree with directions of the  $\dot{\epsilon}_1$  axes computed from the tide-uncorrected ice velocities (Figure 5(a)) with a root mean square deviation (RMSD) of  $24.76^\circ$  (Figure 5(b)). However, the crevasses are approximately parallel to the  $\dot{\epsilon}_1$  axes (Figure 5(c)) with a RMSD of  $8.87^\circ$  (Figure 5(d)). This represents that the crevasses in the hinge zone of CGT were formed by stresses from the gravitational ice flow, rather than by tidal flexure.

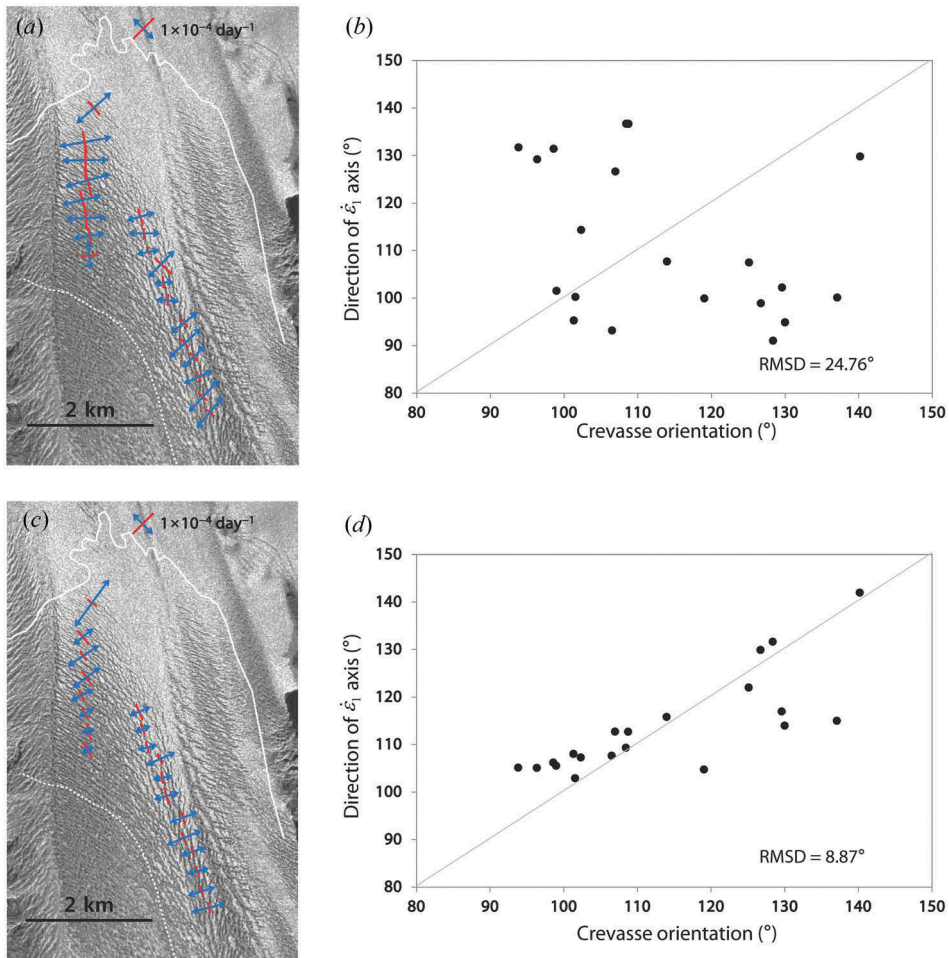


**Figure 5.** Axes of the most (blue arrows) and least (red lines) tensile strain rates at 20 large crevasses in the hinge zone of CGT and the comparisons of the crevasse orientations with the  $\epsilon_1$  axes derived from ((a)–(b)) the tide-uncorrected ice velocities and ((c)–(d)) tide-corrected ice velocities, respectively.

## 5. Conclusion

Surface strain rates of CGT in East Antarctica were derived from tide-corrected ice velocity measured by removing the vertical tidal deflection from the COSMO-SkyMed 1-day DInSAR images. The hinge zone of CGT showed large surface deformation by extension, divergence, lateral shearing, and thinning, especially in a heavy crevassing area, while the freely floating zone showed very small strain rates due to spatially constant ice flow. The crevasses in the hinge zone are parallel to the least tensile (normal to the most tensile) principal strain rate axes calculated from the tide-corrected ice velocity, which represents that the crevasses were formed by the stresses from the gravitational ice flow rather than by tidal flexure. This research showed that the elimination of tidal signals over floating glaciers from DInSAR images is essential to measure the accurate ice velocity and strain rates. The tide-corrected ice velocity and strain rates will thus be of great value in better understating of ice dynamics of floating glaciers.

## Disclosure statement

No potential conflict of interest was reported by the authors.

## Funding

This research was supported by the National Research Foundation of Korea [Grant Numbers: NRF-2013R1A1A2008062 and NRF-2016R1D1A1A09916630], and by the Korea Polar Research Institute (KOPRI) project (PE16040).

## ORCID

Hyangsun Han  <http://orcid.org/0000-0002-0414-519X>

Hoonyol Lee  <http://orcid.org/0000-0002-5980-8640>

## References

- Benn, D. I., N. R. J. Hulton, and R. H. Mottram. 2007. "Calving Laws', 'Sliding Laws' and the Stability of Tidewater Glaciers." *Annals of Glaciology* 46 (1): 123–130. doi:10.3189/172756407782871161.
- Bindschadler, R., P. Vornberger, D. Blankenship, T. Scambos, and R. Jacobel. 1996. "Surface Velocity and Mass Balance of Ice Streams D and E, West Antarctica." *Journal of Glaciology* 42 (142): 461–475.
- Egbert, G. D., and S. Y. Erofeeva. 2002. "Efficient Inverse Modeling of Barotropic Ocean Tides." *Journal of Atmospheric and Oceanic Technology* 19 (2): 183–204. doi:10.1175/1520-0426(2002)019<0183:EIMOBO>2.0.CO;2.
- Fujisada, H., G. B. Bailey, G. G. Kelly, S. Hara, and M. J. Abrams. 2005. "ASTER DEM Performance." *IEEE Transactions on Geoscience and Remote Sensing* 43 (12): 2707–2714. doi:10.1109/TGRS.2005.847924.
- Han, H., Y. Ji, and H. Lee. 2013. "Estimation of Annual Variation of Ice Extent and Flow Velocity of Campbell Glacier in East Antarctica Using COSMO–Skymed SAR Images." *Korean Journal of Remote Sensing* 29 (1): 45–55. doi:10.7780/kjrs.2013.29.1.5.
- Han, H., and H. Lee. 2014. "Tide Deflection of Campbell Glacier Tongue, Antarctica, Analyzed by Double-Differential SAR Interferometry and Finite Element Method." *Remote Sensing of Environment* 141: 201–213. doi:10.1016/j.rse.2013.11.002.
- Han, H., and H. Lee. 2015. "Tide-Corrected Flow Velocity and Mass Balance of Campbell Glacier Tongue, East Antarctica, Derived from Interferometric SAR." *Remote Sensing of Environment* 160: 180–192. doi:10.1016/j.rse.2015.01.014.
- Harper, J. T., N. F. Humphrey, and W. T. Pfeffer. 1998. "Crevasse Patterns and the Strain-Rate Tensor: A High-Resolution Comparison." *Journal of Glaciology* 44 (146): 68–76.
- Nick, F. M., C. J. Van Der Veen, A. Vieli, and D. I. Benn. 2010. "A Physically Based Calving Model Applied to Marine Outlet Glaciers and Implications for the Glacier Dynamics." *Journal of Glaciology* 56 (199): 781–794. doi:10.3189/002214310794457344.
- Padman, L., S. Erofeeva, and I. Joughin. 2003. "Tides of the Ross Sea and Ross Ice Shelf Cavity." *Antarctic Science* 15 (1): 31–40. doi:10.1017/S0954102003001032.
- Price, S. F., and I. M. Whillans. 2001. "Crevasse Patterns at the Onset to Ice Stream B, West Antarctica." *Journal of Glaciology* 47 (156): 29–36. doi:10.3189/172756501781832494.
- Rignot, E., J. Mouginot, and B. Scheuchl. 2011. "Ice Flow of the Antarctic Ice Sheet." *Science* 333 (6048): 1427–1430. doi:10.1126/science.1208336.
- Vaughan, D. G. 1993. "Relating the Occurrence of Crevasses to Surface Strain Rates." *Journal of Glaciology* 39 (132): 255–266.